

ELSEVIER

Journal of Medical Imaging and Radiation Sciences 53 (2022) 374–383

Journal of Medical Imaging  
and Radiation SciencesJournal de l'imagerie médicale  
et des sciences de la radiation[www.elsevier.com/locate/jmir](http://www.elsevier.com/locate/jmir)

## Research Article

Optimal theranostic SPECT imaging protocol for  $^{223}\text{Ra}$  dichloride therapy

Luis Felipe C. Lima<sup>a,\*</sup>, Gabriella M. Pinto<sup>b</sup>, Catherine C.O. da Silva<sup>c</sup>, Dominique C. Fuser<sup>b</sup>,  
Mauricio P. Gama<sup>d</sup>, Cristian F. Griebler<sup>e</sup>, Daniel A.B. Bonifacio<sup>e</sup>, Lidia V. de Sá<sup>e</sup> and  
Ricardo T. Lopes<sup>a</sup>

<sup>a</sup> Nuclear Instrumentation Laboratory (COPPE/UFRJ), Brazil<sup>b</sup> Sao Carlos Oncological Health, Brazil<sup>c</sup> Nuclear Engineering Program (COPPE/UFRJ), Brazil<sup>d</sup> Statistics Federal Council, Brazil<sup>e</sup> Radioprotection Dosimetry Institute (IRD), Brazil

## ABSTRACT

$^{223}\text{Ra}$  dichloride image-based individual dosimetry requires an optimal acquisition and reconstruction protocol and proper image correction methods for theranostic applications. To assess this problem, radium-223 dichloride SPECT images were acquired from a Jaszczak simulator with a dual-headed gamma camera, LEHR collimator,  $128 \times 128$  matrix, and total time of 32 minutes. A cylindrical PMMA phantom was used to calibrate the measurements performed with Jaszczak. The image quality parameters (noise coefficient, contrast, contrast-to-noise ratio and recovery coefficient) and septal penetration correction were calculated by MATLAB®. The best results for the investigated image quality parameters were obtained with an 89 keV energy window (24% wide) produced together with OSEM/MLEM reconstruction (8 subsets and 4 iterations) applying a Butterworth filter (order 10 and cutoff frequency of  $0.48 \text{ cycles} \cdot \text{cm}^{-1}$ ). The successfully performed recovery coefficient parameter evaluation allows uptake correction for future patient dosimetry applications.

## RÉSUMÉ

La dosimétrie individuelle basée sur l'image au dichlorure de radium-223 nécessite un protocole d'acquisition et de reconstruction optimal et des méthodes de correction d'image appropriées pour les applications théranostiques. Pour évaluer ce problème, des images SPECT au dichlorure de radium-223 ont été acquises à partir d'un simulateur Jaszczak avec une caméra gamma à double tête, un collimateur LEHR, une matrice  $128 \times 128$  et une durée totale de 32 minutes. Un fantôme cylindrique en PMMA a été utilisé pour calibrer les mesures effectuées avec le simulateur Jaszczak. Les paramètres de qualité d'image (coefficient de bruit, contraste, rapport contraste/bruit et coefficient de récupération) et la correction de la pénétration septale ont été calculés par MATLAB®. Les meilleurs résultats pour les paramètres de qualité d'image étudiés ont été obtenus avec une fenêtre d'énergie de 89 keV (24 % de largeur) produite conjointement avec une reconstruction OSEM/MLEM (huit sous-ensembles et quatre itérations) appliquant un filtre de Butterworth (ordre 10 et fréquence de coupure de  $0,48 \text{ cycles} \cdot \text{cm}^{-1}$ ). L'évaluation réussie des paramètres du coefficient de récupération permet la correction de l'absorption pour les futures applications de dosimétrie des patients.

Contributors: All authors contributed to the conception or design of the work, the acquisition, analysis, or interpretation of the data. All authors were involved in drafting and commenting on the paper and have approved the final version.

Funding: This study did not receive any specific grant from funding agencies in the public, commercial, or not-for-profit sectors.

Ethical approval: Not required.

Declaration of Competing Interest: All authors declare no conflict of interest.

\* Corresponding author.

E-mail address: [felipelima2005@yahoo.com.br](mailto:felipelima2005@yahoo.com.br) (L.F.C. Lima).

## Introduction

Prostate cancer is the second most frequently diagnosed cancer in the world [1]. Bone metastasis worsens patient welfare, causes pain and high bone fragility, and limits mobility [2,3]. One approach to treat this cancer is to lower testosterone levels in the body to stabilize or reverse the cancer stage. However, when no response is obtained by this treatment, the cancer is named castration-resistant prostate cancer (CRPC) [4–6].

Therapy with radium-223 dichloride ( $^{223}\text{RaCl}_2$ ) has been administered in patients with bone metastases from CRPC [7–9] and in some studies on breast cancer [10,11]. Since radium-223 mimics calcium [11,12], radiopharmaceuticals are captured in bone-formation regions.

Due to alpha emission, radium-223 presents highly localized energy deposition around the original decayed atom and a lethal absorbed dose deposited in cells with high precision [12–14]. In experiments conducted in humans, radium-223 efficacy in extending life expectancy has been demonstrated [9]. An activity of 55 kBq per kilogram of patient weight [15] is recommended, although low myelosuppression was observed with activity ranging from 50 to 250 kBq  $\text{kg}^{-1}$  [16]. In addition, a recent simulation work using Monte Carlo codes in mouse bones [17] showed that the absorbed dose in bone marrow is relatively low. Nevertheless, despite some dosimetric efforts [18,19], as no pretherapy dosimetry is performed in routine clinical practice, the real treatment efficacy for each patient is still unknown.

Thus, one of the necessary steps needed to implement therapy planning by clinical dosimetry in nuclear medicine dosimetry is the development of an optimized protocol of image acquisition and reconstruction so that the biodistribution parameters and residence time of the radiopharmaceutical in each organ and region can be quantifiable.

Approximately 1% of the total energy emitted in radium-223 decay is due to photons [20,21]. Moreover, low photon emission and bremsstrahlung photons severely affect image quality [22,23]. Additionally, due to the production of lead characteristic X-rays [24,25], the collimator thickness directly influences the fraction of detected photons [26].

Despite recently published results [26,27], there are still some efforts to be made toward a clinically viable theranostic approach, such as partial volume effect (PVC) investigation and the appropriate location of the photopeak located between 80 and 90 keV and its window size.

This work aimed to optimize a protocol for the acquisition and reconstruction of SPECT images by analyzing partial volume effects (PVEs) for dosimetric purposes. We expect that this protocol may be used in patients subjected to radium-223 dichloride therapy and implemented in clinical routine for dosimetry purposes in the near future.

## Methods

To perform image quality evaluation, a Jaszczak phantom (ACR) and a PMMA (polymethylmethacrylate) phantom for sensitivity measurement were used. Then, two tests were carried

out with differences in the imaging acquisition protocol with varying energy windows and reconstruction methods, named Tests I and II, and specified as follows.

### Jaszczak ACR phantom

The phantom contains four cylinders of plastic (Fig. 1) to simulate lesion uptake with diameters of 8, 12, 16, and 25 mm and volumes of 2, 4.5, 8, and 19 ml. Additionally, there were three more cylinders with a diameter of 25 mm, two made of plastic to simulate water and air and another made of Teflon to simulate bone tissue. The Jaszczak simulator has a total volume of 6.815 L including the cylinders.

### PMMA phantom for volumetric sensitivity test

The total inserted activity in this cylindrical phantom was 2.035 MBq, yielding a concentration of 8.14 kBq  $\text{ml}^{-1}$ . The purpose was to relate the tested activity with the grayscale value of each pixel in the reconstructed image. Each grayscale pixel  $p_{ij}$  of the slice images has a correspondent radiation count  $c_{ij}$  (linear relation), and therefore, the sum of all  $p_{ij}$  is proportional to the total count in the region of interest  $S_{count}$ . Due to the short examination time (32 minutes) relative to the decay time (half-life of 11 days), the activity during the examination can be considered constant. Since PMMA phantom activity ( $A_{PMMA}$ ) is known, it is possible to compute cylinder  $i$  activity measured by the SPECT system ( $A_{MAc,i}$ ) by computing the sum of pixel values in the cylinder's region of interest ( $S_{MAc,i}$ ). Thus,

$$A_{MAc,i} = \frac{S_{MAc,i}}{S_{PMMA}} A_{PMMA}$$

$S_{PMMA}$  is the sum of pixel values inside the PMMA phantom.

### Gamma camera

All SPECT acquisitions were performed in a dual-headed gamma camera (Millennium MG, General Electric – GE). A low energy high resolution (LEHR) collimator was used due to the high counts previously obtained for radium-223 [26].

### Experimental activity

Based on the radiopharmaceutical manufacturer posology of 55 kBq  $\text{kg}^{-1}$  [15] and Jaszczak total volume, the total theoretical activity to be inserted is 374.82 kBq. From previously published data [7], up to 77% of the injected activity leads to bone absorption, while the remaining 23% circulates in the body. Thus, the maximum uptake percentage was considered the worst-case scenario of the absorbed radiation dose for healthy tissue. Therefore, the theoretical activity concentrations for the Jaszczak cylinders were 8.24 kBq  $\text{mL}^{-1}$  and 0.012 kBq  $\text{mL}^{-1}$  in the simulator body (Fig. 1).

Thus, for Test I, the approximated experimental activity inserted in the cylinders was 8.14 kBq  $\text{mL}^{-1}$ , and no background (BG) activity was inserted in the simulator body. For Test II, the experimental activity concentration inserted in the cylinders was 7.12 kBq  $\text{mL}^{-1}$ , and it was 0.031 kBq  $\text{mL}^{-1}$  inside

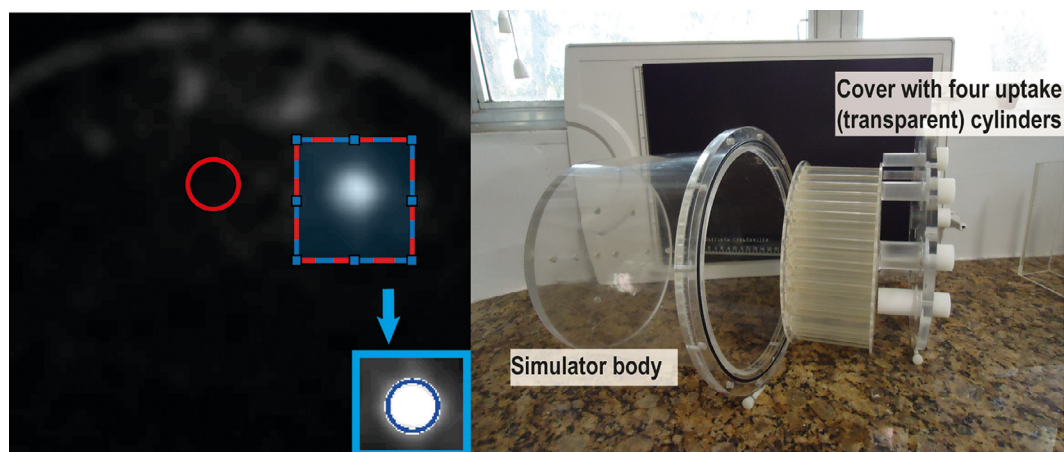


Fig. 1. Slice containing cylinders with activity (left). The selected area (dashed contour in blue and red) indicates the area to be cut. The clipped image is indicated by the arrow with successful circle identification (blue contour around the cylinder). Circular background (BG) region positioning is highlighted in the central phantom region (red). Jaszczak phantom is illustrated at right.

Table 1  
Acquisition and reconstruction parameters for Tests I and II.

Test I			Test II		
Acquisition	Reconstruction		Acquisition	Reconstruction	
Energy window	Filter	Iteration	Energy window	Filter	Iteration
89 keV (24%)	Butterworth	4	89 keV (24%)	Butterworth	2
154 keV (20%)	Hann	8	Triple window	Hann	4
270 (20%)	Gauss 0.5	12			
Triple window	Gauss 1.5				
	Gauss 4.0				

the simulator body. The volumetric sensitivity phantom also received a concentration of  $8.14 \text{ kBq mL}^{-1}$ .

### Acquisition

SPECT images were acquired with a circular orbit and a rotation step of  $2.8125^\circ$  every 30 s ( $180^\circ$  with 64 views for each head) to increase photon statistics and at the same time yield a reasonable total time of 32 min for future patient applications. The matrix used was  $128 \times 128$ , according to a previous study [27]. The LEHR collimator was chosen.

The energy windows applied in Test I were 89 keV (24% wide), 154 keV (20% wide), 270 keV (20% wide), and triple window. This last one takes into account in the same acquisition the three peaks of 89, 154, and 270 keV with their corresponding windows (union of windows for single acquisition). Thus, photons outside these windows do not contribute to the image formation process. The tested window values in Test II were 89 keV (24% wide) and triple window.

### Image reconstruction

The reconstruction method used in every test was OSEM/MLEM with 8 subsets, analyzing different numbers of iterations and applying distinct filters.

### Test I

The applied filters in this first experiment were Butterworth (order 10 and cutoff frequency of  $0.48 \text{ cycles cm}^{-1}$ ), Hann (cutoff frequency of  $0.9 \text{ cycles cm}^{-1}$ ) and three Gaussian filters of FWHM (full width at half maximum) in the XY plane of 0.5, 1.5, and 4.0 pixels and FWHM along the Z-axis of 4.0 pixels. The iteration values were 4, 8, and 12, resulting in 60 reconstruction protocols (Table 1).

### Test II

The most suitable parameters from Test I were selected, resulting in two energies (triple window and 89 keV window) for acquisition, two filters for reconstruction (Butterworth and Hann – same cutoff frequency as in Test I), and number of iterations of 2 and 4 due to previous results [27], yielding 8 reconstruction protocols (Table 1).

### Image correction

Image deconvolution was performed to correct septal penetration and scatter effects with the Richardson-Lucy method and fifteen iterations [28–30]. The MATLAB® *blinddeconv* function was used for this purpose. The image point spread function (PSF) was acquired with the same SPECT acquisition

conditions previously mentioned. The point source used was a 1 mm capillary containing a single drop of radium-223 dichloride solution. The estimated activity was 40 kBq based on the whole measured activity syringe and considering one drop with a rough volume of 0.05 mL. This correction was performed only for Test II due to the low emissions of 154 and 270 keV energy windows.

Deconvolution was performed using PSF and original images with the same acquisition and reconstruction parameters.

### Image quality evaluation

Since the SPECT equipment does not have coupled computed tomography, the precise borders of the four cylinders of Jaszczak's cover (8, 12, 16, and 25 mm) could not be determined by the emission image. Thus, the full width at half maximum (FWHM) was used to determine the 25 mm cylinder diameter in the SPECT image, and the other circle diameters were adjusted proportionally to their diameters according to the following expression:

$$D_i = D_{FWHM,1} \cdot \frac{d_i}{d_1}$$

where  $i = 1, 2, 3$ , and 4 refer to the 25, 16, 12, and 8 mm cylinders, respectively;  $d_i$  is the cylinder  $i$  diameter in millimeters;  $D_i$  is the cylinder  $i$  diameter in pixels;  $d_{FWHM,1}$  is the 25 mm cylinder diameter in pixels measured according to the FWHM of the bright spot in the image; and  $d_{i,mm}$  represents the cylinder diameter in millimeters (mm). The FWHM criterion was also used to determine the cylinder height along the axial axis (which slices from top to bottom containing the cylinders) since it did not disappear suddenly from one slice to the other.

The FWHM was calculated based on the pixel intensity from a profile line for each slice. Along the axial axis, the sum of each pixel value inside the region of interest was computed for each slice to determine the FWHM.

Cylinder detection was performed using the *imfindcircles* function from MATLAB®, based on IEC International Standard 61675-2 [31]. While the FWHM was used to determine the cylinder diameters, this MATLAB® function was used to determine their centers. Each detected cylinder had its corresponding background circle. The BG circles were positioned in a central region between the cylinders of uptake because the peripheral regions could not be visualized (Fig. 1, left).

The image quality parameters evaluated were the noise coefficient (NC), contrast, contrast-to-noise ratio (CNR), and recovery coefficient (RC), which were defined as follows:

$$NC_i = S_i/B_i,$$

$$C_i = P_i/B_i,$$

$$CNR_i = (P_i - B_i)/S_i,$$

$$RC_i = \left( \frac{A_{\text{detected},i} - A_{\text{detected,BG},i}}{A_{\text{inserted},i} - A_{\text{inserted,BG},i}} \right)$$

where

$S_i$  is the standard value of counts inside the BG circle associated with the  $i$ th BG circle;

$B_i$  is the average value of counts inside the BG circle associated with the  $i$ th cylinder;

$P_i$  is the average value of counts inside the  $i$ th cylinder;

$A_{\text{detected},i}$  is the detected activity inside the  $i$ th cylinder;

$A_{\text{detected,BG},i}$  is the background activity detected inside a cylinder with the  $i$ th cylinder volume;

$A_{\text{inserted},i}$  is the true activity inside the  $i$ th cylinder;

$A_{\text{inserted,BG},i}$  is the true background activity inside a cylinder with the  $i$ th cylinder volume and background activity concentration instead.

### Statistical analysis

Statistical analysis was performed with MATLAB® 2020b with a significance level of 0.05. The applied tests were non-parametric since distributions associated with each detected circle were nonnormal. Statistical analysis was performed only for Test II because Test I had no background concentration. One-way analysis of variance (ANOVA) was conducted to check the hypothesis of equality among mean values from each group, and the hypothesis was rejected. To identify differences between groups, Tukey's test was also performed.

## Results

### Test I

To plot the sum of pixel values as a function of iteration number, only the 25 mm cylinder was considered because smaller cylinders were not visible for all reconstruction sets, particularly for 154 and 270 keV energy windows (Fig. 2). As no BG activity was present, the image quality parameters were not quantified for this first test.

Fig. 3 shows the results of the sum of pixel values inside the 25 mm cylinder region of interest ver-

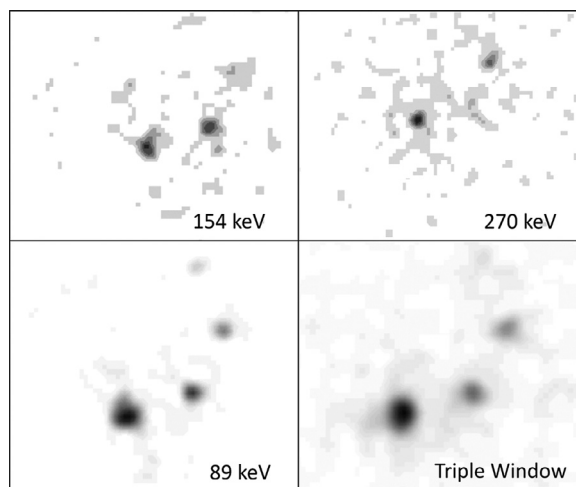


Fig. 2. Slice of highest intake for each energy window reconstructed with Butterworth filter and 4 iterations.



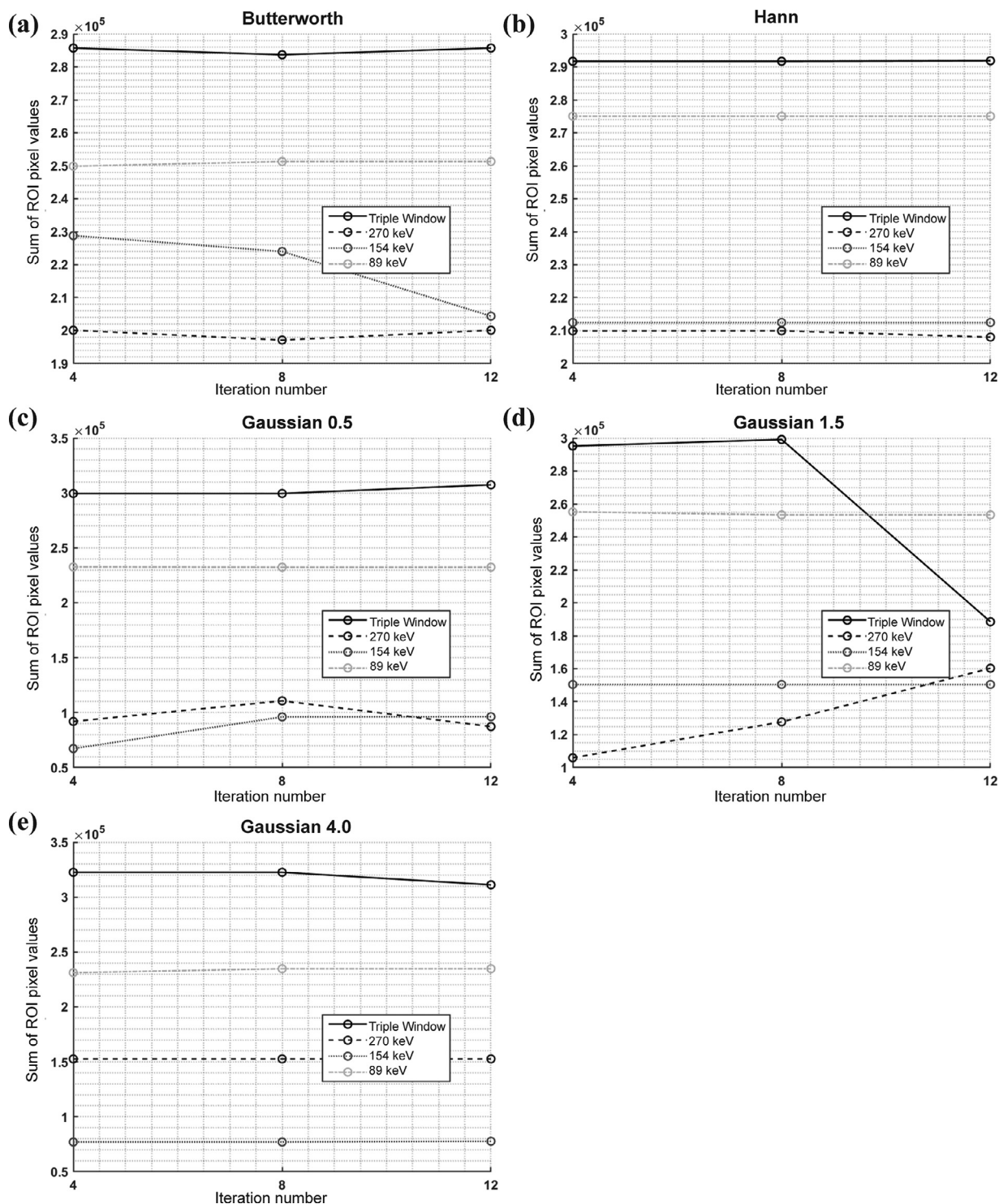


Fig. 3. Sum of pixel values versus iteration number of all energy window tests for the filters: (a) Butterworth, (b) Hann, (c) Gaussian with FWHM of 0.5, (d) Gaussian with FWHM of 1.5, and (e) Gaussian with FWHM of 4.0.

sus iteration number for Test I. The 89 keV window plays a major role in the counts obtained with the triple window.

Table 2 shows the sum of pixel values averaged over iterations for each filter and energy. The last two columns show the relative difference in the energy windows of 154 keV and 270

keV with respect to the 89 keV window. From these values, the Gaussian filters yielded extremely high relative differences when compared with the 89 keV window. This shows that Gaussian filters worsen the image quality when there is low photon emission, which occurs for energy windows of 154 keV and 270 keV (Fig. 2).

Table 2

The sum of pixel values averaged over iterations for each filter and energy is shown in the first four columns. The last two columns show the percent difference of these average values of 154 KeV and 270 keV windows with respect to that of the 89 keV window for each filter, indicated by arrows.

	Triple window	270 keV	154 keV	89 keV	154→89	270→89
Butterworth	285049	199114	219066	250820	13%	21%
Gauss 4.0	318756	152672	77249	233540	67%	35%
Gauss 0.5	302160	96732	86628	232500	63%	58%
Gauss 1.5	260940	131350	150464	253980	41%	48%
Hann	291760	209280	212466	275055	23%	24%

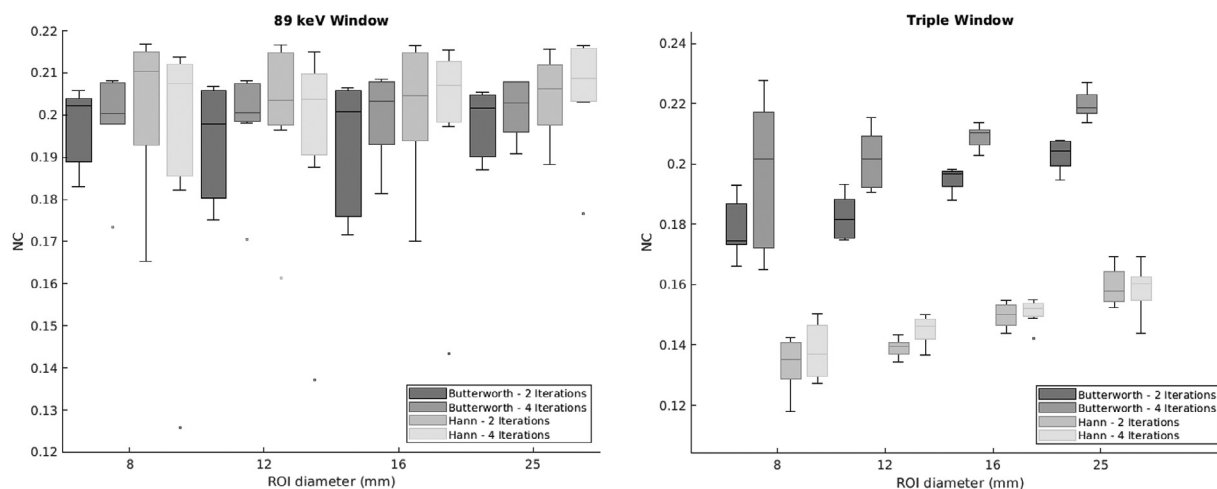


Fig. 4. The graph for both energy windows of noise coefficient – NC shows Whisker boxplots for all filter-iteration combinations.

## Test II

The noise coefficient (Fig. 4) as a function of lesion size exhibited a different behavior for each energy window. The 89 keV window had higher NC values than the triple window. In addition, the iterations exhibited no significant difference between them for the Hann filter. Among these filter-iteration pairs, the Butterworth-2 iterations showed the best result for the 89 keV window (lower NC values). For the triple window, the behavior was opposite, with the Butterworth filter showing superior NC values. Again, the Hann filter had no significant difference between its two iteration options. Additionally, greater interquartile ranges imply a higher background noise influence on the NC value.

Lesion detection is dependent on how distinct it is from background media. Thus, the contrast (Fig. 5) and contrast-to-noise ratio (CNR) (Fig. 6) were evaluated. The best contrast value was obtained by the Butterworth filter and 4 iterations for both energy windows. This filter-iteration pair was significantly different from the other for the 89 keV window. For the triple window, all but the 8 mm lesion filter-iteration pairs were significantly different from the others.

The contrast-to-noise ratio (CNR) has a similar definition as the contrast, except that it includes the noise effect in its calculation. Thus, for the CNR, the Butterworth filter continued to show higher values for the 89 keV window. The Hann filter, however, showed the best values for each cylinder acquired with the triple window except for the smallest cylinder, and

the iteration values were not significantly different from each other.

Finally, the recovery coefficient (RC) was evaluated (Fig. 7). RC quantifies the activity detected by the equipment for each cylinder. An RC less than 1.0 indicates a spill-out effect, while values greater than 1.0 indicate a spill-in effect. The obtained box plots for each cylinder are remarkably close to each other with an extremely small interquartile range for the 89 keV window, which yielded higher RC values. For the other image quality parameters, a significant difference between each filter-iteration pair could not be attested for the 8 mm lesion.

With respect to filters, there was no absolute prevalence for all cylinders. Similarly, the optimal iteration value varied according to the energy window and cylinder considered. The results indicate that 25 mm lesions will be overestimated up to 23% and underestimated up to 97% for 8 mm lesions. This activity detection in SPECT images must be corrected with the appropriate recovery coefficient when calculating absorbed doses of bone metastatic lesions.

## Discussion

In previous experiments, the concentration values differed widely [22,26,27]. The chosen concentration values were based on the clinical routine for CRPC bone metastasis therapy, considering biodistribution information provided by the manufacturer [15] and radiopharmaceutical uptake [7].

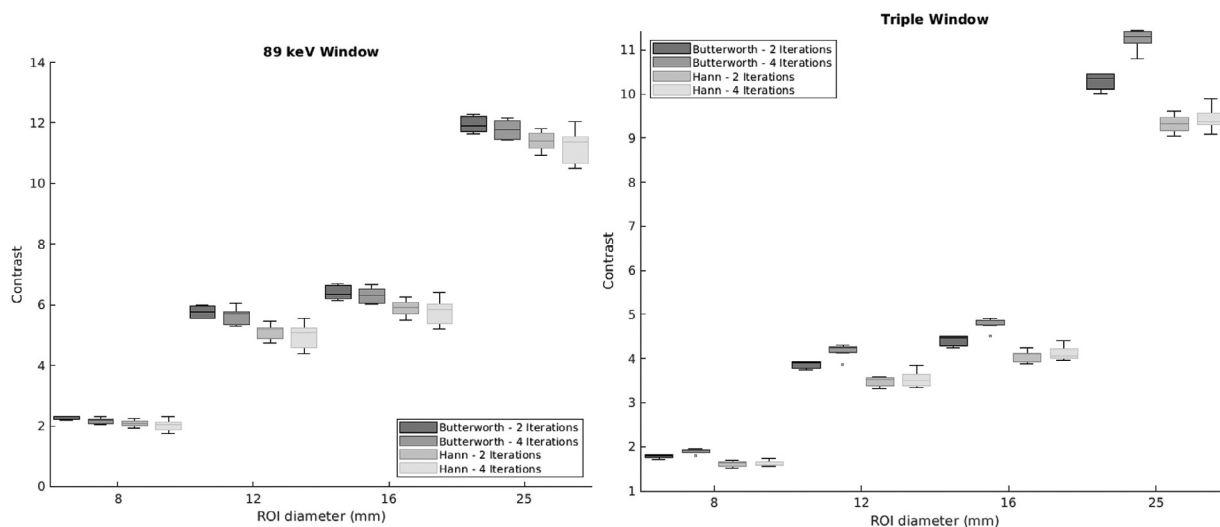


Fig. 5. The graph for both energy windows of contrast shows Whisker boxplots for all filter-iteration combinations.

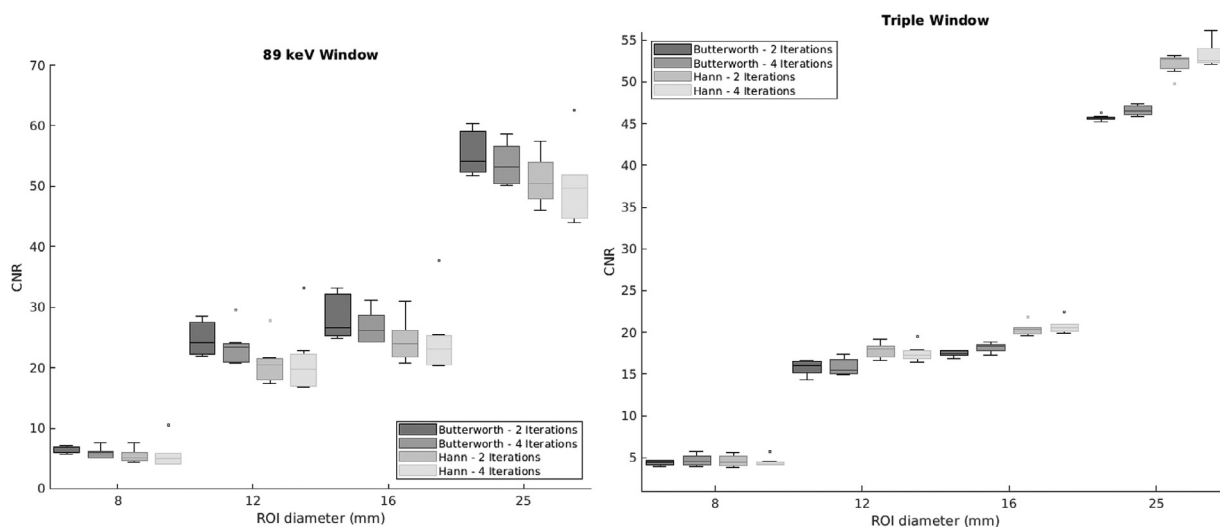


Fig. 6. The graph for both energy windows of contrast-to-noise ratio (CNR) shows Whisker boxplots for all filter-iteration combinations.

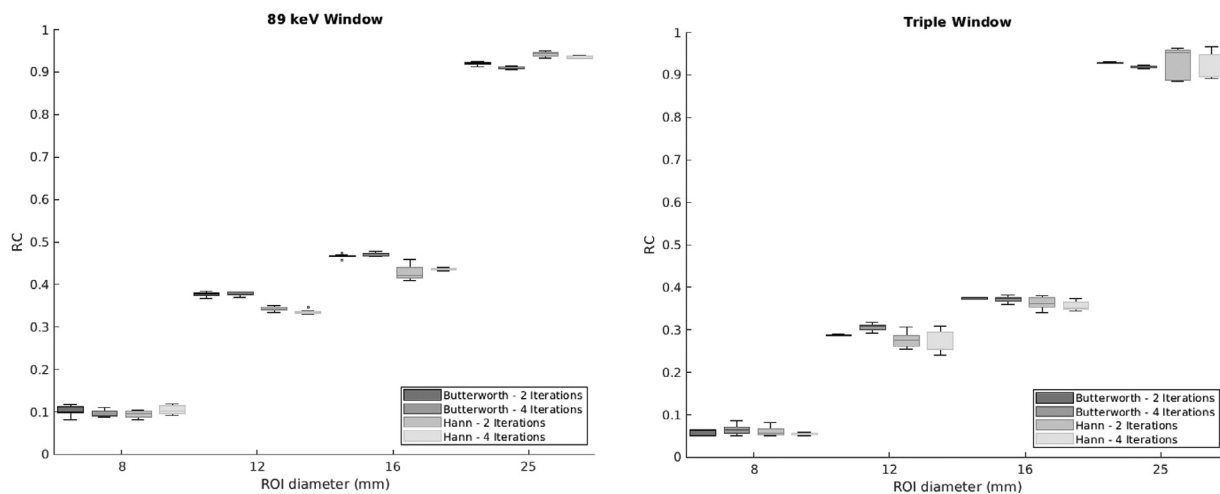


Fig. 7. The graph for both energy windows of recovery coefficient (RC) shows Whisker boxplots for all filter-iteration combinations.

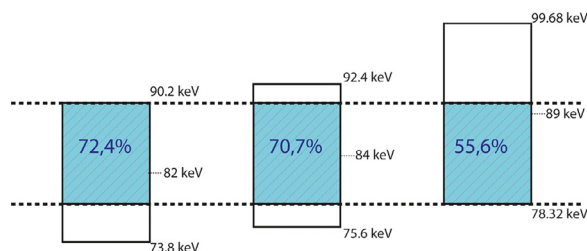


Fig. 8. Comparison of windows and photopeaks used thus far in the literature for photopeaks below 100 keV, namely, from left to right, 82 (20%), 84 (20%), and 89 (24%). The blue hatched region represents the common region and the proportion of this coincidence region to each energy window.

Concerning the energies to perform SPECT examinations, only one study applied more than one energy photopeak [27], and others used double window acquisition (82 and 154 keV with 20% window width) but only planar scintigraphy protocols [32,33] in an attempt to improve radium-223 image quality.

The 89 keV (24%) window was different from those that have been proposed in the literature [22,26]. Fig. 8 illustrates the percentage that this common region (hatched area) represents for the main used windows, which is only 55% for the 89 keV window. The 89 keV photopeak choice was based on a previous study [34], which determined that the optimal acquisition photopeak for radium-223 had to be centered at 89 keV with a 24% wide window to avoid the characteristic X-rays from the lead (inferior window limit) and take advantage of as many emitted photons in the radium-223 decay chain as possible (superior window limit). This energy window option matches the emitted photons with emission probabilities greater than 1% [22] of the radium-223 decay chain absent in the other two [34].

Concerning collimators, LEHR was used here due to the energy windows investigated and its high count rate in comparison with MEGP (Medium Energy General Purpose) and HEGP (High Energy General Purpose) collimators. [26]. To date, LEHR collimators have not been used, mainly due to not providing shielding of characteristic X-rays from the lead of the collimator [26] and, thus, a decrease of image contrast. Nevertheless, the change proposed in this work for the acquisition window (89 keV photopeak and 24% width) favors the LEHR collimator regarding those X-rays. Although the acquisition of a 1 mm capillary without background radiation does not depict clinical reality, it reveals the possibility of obtaining SPECT images from tiny sources with LEHR collimators.

The adopted acquisition matrix was  $128 \times 128$  because considering radium-223 [27], a larger matrix would entail low contrast and more noise, while a smaller matrix would cause loss of spatial resolution. The chosen value in this study was previously used [26]. Additionally, the time per view was fixed to 30 seconds. Although this was not the goal of this work, investigating a shorter total acquisition time is important, especially if we take into account the movement artifacts and common degenerated health condition of the patient.

### Image quality parameters

In Test I, single 154 keV and 270 keV energy window acquisitions were qualitatively discarded for not showing cylinders smaller than 25 mm, mainly for Gaussian filters. The relative uptake difference of these energies compared with the 89 keV window led us to discard Gaussian filters.

Considering Test II, the results for the noise coefficient show invariability regarding cylinder size for the 89 keV window due to the low background value and increasing values for the triple window. Based on the NC definition, background counts from the 89 keV window had a higher standard deviation, implying higher NC values when compared to the triple window.

However, a higher signal-to-noise ratio yielded 89 keV window contrast values approximately twice those for the triple window. Moreover, the Butterworth-4 iteration pair yields the best results for both energy windows (Fig. 5). Also, the low BG values of 89 keV window acquisitions slightly improved the detection of 8 mm lesions.

Observing the CNR graphs, major differences can be observed for the 12 and 16 mm cylinders (Fig. 6) with  $CNR_{89\text{ keV}} > CNR_{Triple}$ . This can be explained by the Hann filter curve shape, which has a more abrupt descent than the Butterworth filter curve shape, making it more prone to deleterious noise effects. This abrupt descent has an inverse effect for the 25 mm cylinder with the triple window, where more signal is preserved in comparison to the Butterworth filter, improving Hann filter performance. However, for the 8 mm cylinder, a convergence of CNR and contrast can be observed for both energy windows due to the lower signal-to-noise ratio (Fig. 5).

The recovery coefficient is important to correct uptake in SPECT images due to *spill-in* and *spill-out* effects. The results from the RC (Fig. 7) show similarity between each filter-iteration pair. Performing an interpolation on each of these curves of the recovery coefficient, lesions with a minimum value of the radius will be fully observed considering that the 89 keV and triple window energies are between 22 and 25 mm depending on the reconstruction set and energy window. In this case, the approximate circular shape of the considered lesion in the observed view (sagittal, coronal, or axial) is implicit.

In addition, for lesions smaller than 0.8 cm, visualization in SPECT examinations from radium-223 emission is less probable. Additionally, the 89 keV window RC values are always higher than those for the triple window, confirming the greater difficulty of observing small lesions for the triple window than for the 89 keV window.

In summary, the energy window is by far the most determinant parameter of image quality. The 89 keV window always showed the best results for all parameters except the noise coefficient.

### Conclusion

Optimization of the acquisition and reconstruction parameters should be considered as the first step to improve the diagno-



sis of bone lesions in patients with castration-resistant prostate cancer.

In this regard, it was shown that sources as thin as a 1 mm capillary can be imaged with the proposed optimized SPECT protocol. Additionally, SPECT acquisition of radium-223 dichloride images can be conducted according to the recommended acquisition parameters of  $128 \times 128$  matrix, LEHR collimator, and centralized photopeak at 89 keV (wide window of 24%). In addition, the reconstruction parameters must be the Butterworth filter (cutoff frequency of 0.48 cycles·cm<sup>-1</sup> and order 10) and 4 iterations.

Precise absorbed dose quantification is important to evaluate treatment efficacy and progress. Therefore, correction of partial volume effects is necessary since the quantification of smaller lesions can result in underestimation of up to 97% in the absorbed dose evaluation. Moreover, the feasibility of the recovery coefficient allows correction of lesion uptake, which is an important move toward future patient dosimetry.

In addition, although LEHR collimator use requires more comparative tests, by performing the proper corrections after acquisition, the LEHR collimator proved able to allow visualization and quantification of all image quality parameters and should be considered a reliable possibility in future studies.

## Supplementary materials

Supplementary material associated with this article can be found, in the online version, at doi:[10.1016/j.jmir.2022.06.009](https://doi.org/10.1016/j.jmir.2022.06.009).

## References

- Bray F, Ferlay J, Soerjomataram I, Siegel RL, Torre LA, Jemal A. Global cancer statistics 2018: GLOBOCAN estimates of incidence and mortality worldwide for 36 cancers in 185 countries. *CA Cancer J Clin*. 2018. doi:[10.3322/caac.21492](https://doi.org/10.3322/caac.21492).
- Cecchini MG, Wetterwald A, van der Pluijm G, Thalmann GN. Molecular and biological mechanisms of bone metastasis. *EAU Updat Ser*. 2005. doi:[10.1016/j.euus.2005.09.006](https://doi.org/10.1016/j.euus.2005.09.006).
- Macedo F, Ladeira K, Pinho F, Saraiva N, Bonito N, Pinto L, et al. Bone metastases: an overview. *Oncol Rev*. 2017;11. doi:[10.4081/oncol.2017.321](https://doi.org/10.4081/oncol.2017.321).
- Feldman BJ, Feldman D. The development of androgen-independent prostate cancer. *Nat Rev Cancer*. 2001. doi:[10.1038/35094009](https://doi.org/10.1038/35094009).
- Sun S, Sprenger CCT, Vessella RL, Haugk K, Soriano K, Mostaghel EA, et al. Castration resistance in human prostate cancer is conferred by a frequently occurring androgen receptor splice variant. *J Clin Invest*. 2010. doi:[10.1172/JCI41824](https://doi.org/10.1172/JCI41824).
- Tennakoon JB, Shi Y, Han JJ, Tsouko E, White MA, Burns AR, et al. Androgens regulate prostate cancer cell growth via an AMPK-PGC-1 $\alpha$ -mediated metabolic switch. *Oncogene*. 2014. doi:[10.1038/ncr.2013.463](https://doi.org/10.1038/ncr.2013.463).
- Kairemo K, Joensuu T, Rasulo N, Kiljunen T, Kangasmäki A. Evaluation of alpha-therapy with radium-223-dichloride in castration resistant metastatic prostate cancer—the role of gamma scintigraphy in dosimetry and pharmacokinetics. *Diagnostics*. 2015;5:358–368. doi:[10.3390/diagnostics5030358](https://doi.org/10.3390/diagnostics5030358).
- Sartor O, Coleman R, Nilsson S, Heinrich D, Helle SI, O'Sullivan JM, et al. Effect of radium-223 dichloride on symptomatic skeletal events in patients with castration-resistant prostate cancer and bone metastases: results from a phase 3, double-blind, randomised trial. *Lancet Oncol*. 2014. doi:[10.1016/S1470-2045\(14\)70183-4](https://doi.org/10.1016/S1470-2045(14)70183-4).
- Parker C, Nilsson S, Heinrich D, Helle SI, O'Sullivan JM, Fosså SD, et al. Alpha emitter radium-223 and survival in metastatic prostate cancer. *N Engl J Med*. 2013. doi:[10.1056/NEJMoa1213755](https://doi.org/10.1056/NEJMoa1213755).
- Takalkar A, Paryani B, Adams S, Subbiah V. Radium-223 dichloride therapy in breast cancer with osseous metastases. *BMJ Case Rep*. 2015. doi:[10.1136/bcr-2015-211152](https://doi.org/10.1136/bcr-2015-211152).
- Coleman R, Aksnes AK, Naume B, Garcia C, Jerusalem G, Piccart M, et al. A phase IIa, nonrandomized study of radium-223 dichloride in advanced breast cancer patients with bone-dominant disease. *Breast Cancer Res Treat*. 2014. doi:[10.1007/s10549-014-2939-1](https://doi.org/10.1007/s10549-014-2939-1).
- Lewington VJ. Bone-seeking radionuclides for therapy. *J Nucl Med*. 2005.
- Sgouras G, Roeske JC, McDevitt MR, Palm S, Allen BJ, Fisher DR, et al. MIRD Pamphlet No. 22 (Abridged): radiobiology and dosimetry of  $\alpha$ -particle emitters for targeted radionuclide therapy. *J Nucl Med*. 2010;51:311–328. doi:[10.2967/jnumed.108.058651](https://doi.org/10.2967/jnumed.108.058651).
- Yeong C-H, Cheng M, Ng K-H. Therapeutic radionuclides in nuclear medicine: current and future prospects. *J Zhejiang Univ Sci B*. 2014. doi:[10.1007/978-3-319-46859-4\\_3](https://doi.org/10.1007/978-3-319-46859-4_3).
- Xofigo. *Cloreto de Rádio (223 Ra)*. Anvisa. Bayer Healthc Pharm Inc; 2018.
- Nilsson S, Larsen RH, Fosså SD, Balteskard L, Borch KW, Westlin JE, et al. First clinical experience with  $\alpha$ -emitting radium-223 in the treatment of skeletal metastases. *Clin Cancer Res*. 2005. doi:[10.1158/1078-0432.CCR-04-2244](https://doi.org/10.1158/1078-0432.CCR-04-2244).
- Pinto GM, Bonifacio DAB, De Sá LV, Lima LFC, Vieira IF, Lopes RT. A cell-based dosimetry model for radium-223 dichloride therapy using bone micro-CT images and GATE simulations. *Phys Med Biol*. 2020. doi:[10.1088/1361-6560/ab6b42](https://doi.org/10.1088/1361-6560/ab6b42).
- Allen B. Clinical trials of targeted alpha therapy for cancer. *Rev Recent Clin Trials*. 2008. doi:[10.2174/157488708785700339](https://doi.org/10.2174/157488708785700339).
- Jiang W, Ulmert D, Simons BW, Abou DS, Thorek DLJ. The impact of age on radium-223 distribution and an evaluation of molecular imaging surrogates. *Nucl Med Biol*. 2018;62–63:1–8. doi:[10.1016/j.nucmedbio.2018.05.003](https://doi.org/10.1016/j.nucmedbio.2018.05.003).
- European Medicines Agency Annex I summary of product characteristics-Xofigo. *Bayer. Sci Med Heal*. 2013.
- ØS Bruland, S Nilsson, Fisher DR, Larsen RH, Vessella Weilbaeher, et al. High-linear energy transfer irradiation targeted to skeletal metastases by the  $\alpha$ -emitter 223Ra: Adjuvant or alternative to conventional modalities? *Clin Cancer Res*. 2006. doi:[10.1158/1078-0432.CCR-06-0841](https://doi.org/10.1158/1078-0432.CCR-06-0841).
- Hindorf C, Chittenden S, Aksnes A, Parker C, Flux GD. Quantitative imaging of 223 Ra-chloride (Alpharadin) for targeted alpha-emitting radionuclide therapy of bone metastases 2012:0–6. <https://doi.org/10.1097/MNM.0b013e328353bb6e>.
- Bushberg JT, Seibert JA, Leidholdt Jr EM, Boone JM. The Essential Physics of Medical Imaging. 2nd ed. 2002. ISBN:978-0-7817-8057-5.
- Delgado JU, Morel J, Etcheverry M. Measurements of photon emission probabilities from the decay of 226Ra and daughters. *Appl Radiat Isot*. 2002. doi:[10.1016/S0969-8043\(01\)00179-8](https://doi.org/10.1016/S0969-8043(01)00179-8).
- Simões RFP, Da Silva CJ, Da Silva RL, Poledna R, Da Cruz PAL, De Sá LV. Deconvolution method to split up X-ray peaks emitted by 223Ra. *Brazilian J Radiat Sci*. 2018. doi:[10.15392/bjrs.v6i1.353](https://doi.org/10.15392/bjrs.v6i1.353).
- Owaki Y, Nakahara T, Kosaka T, Fukada J, Kumabe A, Ichimura A, et al. Ra-223 SPECT for semi-quantitative analysis in comparison with Tc-99m HMDP SPECT: phantom study and initial clinical experience. *EJNMMI Res*. 2017;7. doi:[10.1186/s13550-017-0330-z](https://doi.org/10.1186/s13550-017-0330-z).
- Benabdallah N, Bernardini M, Bianciardi M, de Labriolle-Vaylet C, Franck D, Desbrée A. 223 Ra-dichloride therapy of bone metastasis: optimization of SPECT images for quantification. *EJNMMI Res*. 2019. doi:[10.1186/s13550-019-0488-7](https://doi.org/10.1186/s13550-019-0488-7).
- Barrack F, Scuffham J, McQuaid S. Septal penetration correction in I-131 imaging following thyroid cancer treatment. *Phys Med Biol*. 2018. doi:[10.1088/1361-6560/aab13a](https://doi.org/10.1088/1361-6560/aab13a).

- [29] Teo BK, Seo Y, Bacharach SL, Carrasquillo JA, Libutti SK, Shukla H, et al. Partial-volume correction in PET: Validation of an iterative postreconstruction method with phantom and patient data. *J Nucl Med*. 2007;48:802–810. doi:[10.2967/jnumed.106.035576](https://doi.org/10.2967/jnumed.106.035576).
- [30] Boussion N, Cheze Le Rest C, Hatt M, Visvikis D. Incorporation of wavelet-based denoising in iterative deconvolution for partial volume correction in whole-body PET imaging. *Eur J Nucl Med Mol Imaging*. 2009;36:1064–1075. doi:[10.1007/s00259-009-1065-5](https://doi.org/10.1007/s00259-009-1065-5).
- [31] IECIEC 61675-2: Radionuclide imaging devices - Characteristics and test conditions - Part 2: Gamma cameras for planar, wholebody, and SPECT imaging. *IEC*. 2015;61675-2:61.
- [32] Pacilio M, Cassano B, Chiesa C, Giancola S, Ferrari M, Pettinato C, et al. Physica medica the Italian multicentre dosimetric study for lesion dosimetry in  $^{223}\text{Ra}$  therapy of bone metastases : calibration protocol of gamma cameras and patient eligibility criteria. *Phys Medica*. 2016;32:1731–1737. doi:[10.1016/j.ejmp.2016.09.013](https://doi.org/10.1016/j.ejmp.2016.09.013).
- [33] Pacilio M, Ventroni G, De Vincentis G, Cassano B, Pellegrini R, Di Castro E, et al. Dosimetry of bone metastases in targeted radionuclide therapy with alpha-emitting  $^{223}\text{Ra}$ -dichloride. *Eur J Nucl Med Mol Imaging*. 2016;43:21–33. doi:[10.1007/s00259-015-3150-2](https://doi.org/10.1007/s00259-015-3150-2).
- [34] Simões RFP. Padronização Absoluta do Ra-223 e Calibração dos Sistemas de Referência do LNMRI. IRD - Radioprotection and Dosimetry Institute, 2018.